





Analyzing Black-Hole Ringdowns with Orthonormal Modes

Soichiro Morisaki ¹, Hayato Motohashi ², Motoki Suzuki ^{3,1} and Daiki Watarai ^{3,4}

¹*Institute for Cosmic Ray Research, The University of Tokyo,*

5-1-5 Kashiwanoha, Kashiwa, Chiba 277-8582, Japan

²*Department of Physics, Tokyo Metropolitan University,*

1-1 Minami-Osawa, Hachioji, Tokyo 192-0397, Japan

³*Department of Physics, Graduate School of Science,*

The University of Tokyo, 7-3-1 Hongo, Bunkyo-ku, Tokyo 113-8655, Japan

⁴*Research Center for the Early Universe (RESCEU),*

Graduate School of Science, The University of Tokyo, Tokyo 113-0033, Japan

The ringdown signal following a black hole (BH) merger can be modeled as a superposition of BH quasinormal modes (QNMs), offering a clean setup for testing gravitational theories. In particular, detecting multiple QNMs enables consistency checks of their frequencies and damping times, serving as a test of General Relativity—a technique known as black hole spectroscopy. However, incorporating additional QNMs introduces challenges such as increased parameter correlations and higher computational costs in data analysis. To address this, we propose an efficient Bayesian analysis method that applies the Gram–Schmidt algorithm to the QNMs. This reduces the correlation between the modes and enables analytic marginalization over the mode amplitudes. We validate our approach using damped sinusoids and numerical waveforms from the Simulating eXtreme Space-times (SXS) catalog.

I. INTRODUCTION

Since the first direct detection of gravitational waves (GWs), the number of detections has increased rapidly over the past decade. The LIGO–Virgo–KAGRA collaboration (LVK) reported 90 GW signals observed until the end of its third observing run (O3) [1–4], with hundreds of additional significant event candidates identified in the ongoing fourth observing run (O4). Most of these signals are consistent with GWs emitted by mergers of binary black holes (BBHs). These detections provide valuable insights into the properties of gravity in the strong-field regime [2, 4–7].

In particular, the ringdown part of GW signal, which is emitted while the merger remnant is settling down to a single rotating black hole, provides a clean setting for testing gravitational theories. At the linear order, it can be modeled as a superposition of damped sinusoids, referred to as quasinormal modes (QNMs). Each mode is labeled by a set of integers, (l, m, n) , where (l, m) are two angular numbers and n is an overtone index that orders modes by decreasing damping time. In General Relativity (GR), the frequency and damping time of each QNM depend solely on the mass and spin of the remnant black hole, allowing these parameters to be estimated from QNM measurements [8]. A simple test of GR is to compare the remnant mass and spin inferred from the ringdown with those independently estimated from the pre-merger part to check their consistency [9–11].

If multiple QNMs are observed, an alternative approach is to check the consistency of their frequencies and damping times, known as black hole (BH) spectroscopy [12–15]. This technique offers a relatively clean test of GR, as it does not rely on detailed waveform modeling. Detecting modes beyond the dominant $(l, |m|, n) = (2, 2, 0)$ mode, however, requires a high signal-to-noise

ratio. Nevertheless, evidence for additional modes has been reported in several events [2, 4, 16–18].

A notable case is GW150914 [19]. Isi et al. analyzed GW150914 incorporating overtones ($n > 0$) and found evidence of at least one overtone for $l = m = 2$ with 3.6σ confidence [16]. While they fit the data starting from the signal peak, where the QNM approximation may not be strictly valid, their analysis, including overtones, yields mass and spin estimations consistent with those from the full inspiral-merger-ringdown analysis. Furthermore, their BH spectroscopy analysis found the observed QNMs to be consistent with the predictions of GR. Subsequent studies by other groups have revisited these findings, with some reporting reduced evidence for overtones compared to the original analysis [20–25]. The validity of fitting data from the signal peak using QNMs, particularly regarding the stability of the fitting, has also been the subject of discussion in the literature [26–33].

For accurate inference, it is desirable to include as many QNMs as possible. However, increasing the number of included modes also increases the number of model parameters, making the analysis more complex and computationally expensive. Moreover, since QNMs are not orthogonal, correlations between modes make it challenging to unambiguously identify which modes are present in the data, especially when many modes are involved.

In this paper, we propose an efficient method for ringdown inference involving multiple QNMs. Specifically, we employ the Gram–Schmidt procedure to orthonormalize the QNM basis and sample the mode coefficients using a prior that is uniform in their amplitudes. This parameterization and prior choice offer two key advantages. First, the mode coefficients can be analytically marginalized over, substantially reducing the dimensionality of the inference problem and lowering computational cost. Second, orthonormalization mitigates corre-

lations between mode coefficients, enhancing the robustness of mode identification. We note that several authors have previously proposed alternative methods for analytically marginalizing over mode amplitudes [23, 34]. Furthermore, the application of the Gram–Schmidt algorithm to the QNM basis was explored in a different context in [35].

This paper is organized as follows. Section II reviews the ringdown waveform model and time-domain Bayesian analysis framework. In Sec. III, we introduce our analysis method. Sections IV and V present validation of our method using both damped sinusoids and numerical relativity waveforms from the Simulating eXtreme Space-times (SXS) catalog. Finally, Section VI summarizes our conclusions.

II. TIME-DOMAIN BAYESIAN FRAMEWORK FOR ANALYZING RINGDOWN

In this section, we introduce the signal model we employ in this work and review a time-domain Bayesian method to infer signal parameters.

A. Signal model

Let $h(t)$ denote complex GW strain,

$$h(t) = h_+(t) + ih_\times(t), \quad (1)$$

where $h_+(t)$ and $h_\times(t)$ are plus and cross polarizations of GWs, respectively. The ringdown signal is modeled as a superposition of damped sinusoids labeled by a set of indices $\alpha = (l, m, n)$ [13, 36],

$$h(t) = \sum_{\alpha} \left[\mathcal{C}_{\alpha} e^{-i\tilde{\omega}_{\alpha} t} S_{\alpha}(\iota, \phi) + \mathcal{C}'_{\alpha} e^{i\tilde{\omega}_{\alpha}^* t} S_{\alpha'}(\iota, \phi) \right], \quad (2)$$

where \mathcal{C}_{α} and \mathcal{C}'_{α} are complex mode amplitudes, $\tilde{\omega}_{\alpha} = \omega_{\alpha} - i/\tau_{\alpha}$ is the complex frequency dependent on the remnant BH's mass and spin, M_f and χ_f . $S_{\alpha}(\iota, \phi)$ is the spin-weighted spheroidal harmonics with the spin weight of -2 , dependent on polar and azimuthal angles ι and ϕ , and $\alpha' = (l, -m, n)$. The summation runs over $\alpha = (l, m, n)$ with $\sum_{\alpha} = \sum_{l=2}^{\infty} \sum_{m=-l}^l \sum_{n=0}^{\infty}$. Here, the summation does not group QNMs based on their angular dependence, but is instead reorganized so that the terms with $m > 0$ correspond to prograde modes, while those with $m < 0$ correspond to retrograde modes. The overtone index n orders QNMs for a given l and m by decreasing decay time, i.e., $\tau_{lm(n+1)} < \tau_{lmn}$, at $\chi_f = 0$.

Let I be the index of the detector. The gravitational wave strain observed in the I -th detector is given by

$$h^I(t) = \text{Re} [F^I h(t - t_S^I)], \quad (3)$$

where $F^I = F_+^I - iF_{\times}^I$ represents the complex beam pattern of the I -th detector and t_S^I is the analysis start time

at the I -th detector. Substituting Eq. (2) into Eq. (3), we obtain

$$h^I(t) = \sum_{\alpha} \sum_{j=0}^3 c_{j,\alpha} v_{j,\alpha}^I(t), \quad (4)$$

where

$$c_{0,\alpha} = \text{Re} [\mathcal{C}_{\alpha} S_{\alpha}(\iota, \phi) + \mathcal{C}'_{\alpha} S_{\alpha'}(\iota, \phi)], \quad (5)$$

$$c_{1,\alpha} = \text{Im} [\mathcal{C}_{\alpha} S_{\alpha}(\iota, \phi) - \mathcal{C}'_{\alpha} S_{\alpha'}(\iota, \phi)], \quad (6)$$

$$c_{2,\alpha} = \text{Im} [\mathcal{C}_{\alpha} S_{\alpha}(\iota, \phi) + \mathcal{C}'_{\alpha} S_{\alpha'}(\iota, \phi)], \quad (7)$$

$$c_{3,\alpha} = \text{Re} [-\mathcal{C}_{\alpha} S_{\alpha}(\iota, \phi) + \mathcal{C}'_{\alpha} S_{\alpha'}(\iota, \phi)], \quad (8)$$

and

$$v_{0,\alpha}^I(t) = F_+^I e^{-\frac{t-t_S^I}{\tau_{\alpha}}} \cos(\omega_{\alpha}(t - t_S^I)), \quad (9)$$

$$v_{1,\alpha}^I(t) = F_+^I e^{-\frac{t-t_S^I}{\tau_{\alpha}}} \sin(\omega_{\alpha}(t - t_S^I)), \quad (10)$$

$$v_{2,\alpha}^I(t) = F_{\times}^I e^{-\frac{t-t_S^I}{\tau_{\alpha}}} \cos(\omega_{\alpha}(t - t_S^I)), \quad (11)$$

$$v_{3,\alpha}^I(t) = F_{\times}^I e^{-\frac{t-t_S^I}{\tau_{\alpha}}} \sin(\omega_{\alpha}(t - t_S^I)). \quad (12)$$

Throughout this work, we assume the coefficients $c_{j,\alpha}$ are free parameters that can take arbitrary real values, without imposing any specific amplitude model. The angular dependence on ι and ϕ is fully absorbed into $\{c_{j,\alpha}\}$. Similarly, although the beam pattern F^I depends on the polarization angle ψ via $F^I(\psi) = F^I(\psi=0)e^{2i\psi}$, this dependence is also absorbed into $\{c_{j,\alpha}\}$. Following previous works [2, 4, 16], we fix the sky location, α and δ , whose values are typically determined based on the information provided by the inspiral-merger-ringdown analysis. Thus, the beam pattern F^I is treated as a fixed quantity.

The analysis start time t_S^I is also fixed. Typically, the start time at a reference detector is fixed near the signal peak time, and the start times at the other detectors are determined by the time delays computed from the fixed sky location. Consequently, the signal model is fully characterized by the remnant BH's mass and spin, M_f and χ_f , and the set of real coefficients $\{c_{j,\alpha}\}$.

In real analyses, only a finite number of QNMs are considered, under the assumption that contributions from the others are negligible. Let K denote the number of included QNMs, indexed as $\{\alpha_0, \alpha_1, \dots, \alpha_{K-1}\}$. In this notation, we assume that QNMs are ordered by significance—i.e., modes with α_{k+1} are less significant than those with α_k . In our demonstration presented in later sections, α_0 represents the dominant $(2, 2, 0)$, while α_k with $k > 0$ denotes the overtones for $l = m = 2$, $\alpha_k = (2, 2, k)$.

When data are available from a single detector, or when detectors are nearly co-aligned, $v_{2,\alpha}^I(t)$ and $v_{3,\alpha}^I(t)$ become degenerate with $v_{0,\alpha}^I(t)$ and $v_{1,\alpha}^I(t)$. In such cases, we set $c_{2,\alpha} = c_{3,\alpha} = 0$, retaining only two coefficients per mode. Let $D = 2$ or 4 denote the number of coefficients used per mode. The resulting model becomes:

$$h^I(t) = \sum_{k=0}^{K-1} \sum_{j=0}^{D-1} c_{j,\alpha_k} v_{j,\alpha_k}^I(t). \quad (13)$$

Thus, the set of real parameters in the analysis consists of $K \times D$ real coefficients:

$$\{c_{j,\alpha_k} | j = 0, \dots, D-1; k = 0, \dots, K-1\}.$$

For brevity, we refer to this set as $\{c_{j,\alpha_k}\}$ throughout the text.

It is worth noting that $c_{j,\alpha}$ corresponds to $x_{+/\times}$ and $y_{+/\times}$ in [36]. The relation between this and other parameterizations of GW polarizations are discussed in [37].

B. Bayesian inference with time-domain likelihood

Next, we review a Bayesian method to infer the signal parameters, $\theta = \{M_f, \chi_f\} \cup \{c_{j,\alpha_k}\}$. The posterior probability density function of θ is computed via Bayes' theorem,

$$p(\theta) = \frac{\pi(\theta)\mathcal{L}(\theta)}{\mathcal{Z}}, \quad (14)$$

where $\pi(\theta)$ is the prior probability density function, $\mathcal{L}(\theta)$ is the likelihood function, and \mathcal{Z} is the evidence, serving as a normalization constant.

Following [36], we employ a time-domain likelihood function given by:

$$\ln \mathcal{L}(\theta) = -\frac{1}{2} \sum_I (\mathbf{d}^I - \mathbf{h}^I(\theta))^T (R^I)^{-1} (\mathbf{d}^I - \mathbf{h}^I(\theta)). \quad (15)$$

Here, \mathbf{d}^I and $\mathbf{h}^I(\theta)$ represent vectors consisting of data and waveform values, respectively, for the I -th detector:

$$\mathbf{d}^I \equiv \begin{pmatrix} d^I(t_0^I) \\ d^I(t_1^I) \\ d^I(t_2^I) \\ \vdots \end{pmatrix}, \quad \mathbf{h}^I(\theta) \equiv \begin{pmatrix} h^I(t_0^I; \theta) \\ h^I(t_1^I; \theta) \\ h^I(t_2^I; \theta) \\ \vdots \end{pmatrix}, \quad (16)$$

where t_i^I represents the i -th time sample of the I -th detector. The components of the matrix R^I are given by the noise auto-correlation function evaluated at the time lag between samples:

$$[R^I]_{ij} = R^I(|t_i^I - t_j^I|). \quad (17)$$

As in many previous studies, we assume that the prior is separable:

$$\pi(\theta) = \pi(M_f, \chi_f) \pi(\{c_{j,\alpha_k}\}). \quad (18)$$

Typically, $\pi(M_f, \chi_f)$ is taken to be uniform over a broad range of M_f and χ_f . On the other hand, several different forms of $\pi(\{c_{j,\alpha_k}\})$ have been proposed and employed in the literature [2, 17, 36, 37].

III. RINGDOWN ANALYSIS WITH ORTHONORMAL MODES

In this section, we introduce our semi-analytic analysis method. As a preparatory step, we first rewrite the likelihood function. We define concatenated data and waveform vectors across all detectors:

$$\mathbf{d} \equiv \begin{pmatrix} \mathbf{d}^{I_0} \\ \mathbf{d}^{I_1} \\ \mathbf{d}^{I_2} \\ \vdots \end{pmatrix}, \quad \mathbf{h}(\theta) \equiv \begin{pmatrix} \mathbf{h}^{I_0}(\theta) \\ \mathbf{h}^{I_1}(\theta) \\ \mathbf{h}^{I_2}(\theta) \\ \vdots \end{pmatrix}. \quad (19)$$

We also introduce the block-diagonal noise correlation matrix:

$$R = \begin{pmatrix} R^{I_0} & 0 & 0 & \dots \\ 0 & R^{I_1} & 0 & \dots \\ 0 & 0 & R^{I_2} & \dots \\ \vdots & \vdots & \vdots & \ddots \end{pmatrix}. \quad (20)$$

With these variables, the logarithm of likelihood takes the following form,

$$\ln \mathcal{L}(\theta) = -\frac{1}{2} (\mathbf{d} - \mathbf{h}(\theta))^T R^{-1} (\mathbf{d} - \mathbf{h}(\theta)) \quad (21)$$

$$= \mathbf{d}^T R^{-1} \mathbf{h}(\theta) - \frac{1}{2} \mathbf{h}(\theta)^T R^{-1} \mathbf{h}(\theta) + \text{const.} \quad (22)$$

Let $\mathbf{v}_{j,\alpha}^I$ be a vector consisting of $v_{j,\alpha}^I(t)$ evaluated at the time samples $\{t_i^I\}$:

$$\mathbf{v}_{j,\alpha}^I = \begin{pmatrix} v_{j,\alpha}^I(t_0^I) \\ v_{j,\alpha}^I(t_1^I) \\ v_{j,\alpha}^I(t_2^I) \\ \vdots \end{pmatrix}. \quad (23)$$

We then define the concatenated vector over all detectors:

$$\mathbf{v}_{j,\alpha} = \begin{pmatrix} \mathbf{v}_{j,\alpha}^{I_0} \\ \mathbf{v}_{j,\alpha}^{I_1} \\ \mathbf{v}_{j,\alpha}^{I_2} \\ \vdots \end{pmatrix}. \quad (24)$$

Equation (13) implies that the concatenated waveform vector $\mathbf{h}(\theta)$ can be expressed as a linear combination of these basis vectors,

$$\mathbf{h}(\theta) = \sum_{k=0}^{K-1} \sum_{j=0}^{D-1} c_{j,\alpha_k} \mathbf{v}_{j,\alpha_k} = V \mathbf{c}, \quad (25)$$

where

$$V = (\mathbf{v}_{0,\alpha_0}, \dots, \mathbf{v}_{D-1,\alpha_0}, \mathbf{v}_{0,\alpha_1}, \dots, \mathbf{v}_{D-1,\alpha_{K-1}}), \quad (26)$$

$$\mathbf{c} = (c_{0,\alpha_0}, \dots, c_{D-1,\alpha_0}, c_{0,\alpha_1}, \dots, c_{D-1,\alpha_{K-1}})^T. \quad (27)$$

Substituting Eq. (25) into Eq. (22), we obtain

$$\ln \mathcal{L}(\theta) = \mathbf{d}^T R^{-1} V \mathbf{c} - \frac{1}{2} \mathbf{c}^T V^T R^{-1} V \mathbf{c} + \text{const.} \quad (28)$$

A. Gram–Schmidt orthogonalization

We perform Gram–Schmidt orthogonalization of the basis vectors \mathbf{v}_{j,α_k} with respect to the inner product defined by,

$$(\mathbf{v}_{j,\alpha_k}, \mathbf{v}_{j',\alpha_{k'}}) = \mathbf{v}_{j,\alpha_k}^T \mathbf{R}^{-1} \mathbf{v}_{j',\alpha_{k'}}. \quad (29)$$

This procedure yields an orthonormal set of basis vectors $\tilde{\mathbf{v}}_{j,\alpha_k}$, which we assemble into the matrix,

$$\tilde{\mathbf{V}} = (\tilde{\mathbf{v}}_{0,\alpha_0}, \dots, \tilde{\mathbf{v}}_{D-1,\alpha_0}, \tilde{\mathbf{v}}_{0,\alpha_1}, \dots, \tilde{\mathbf{v}}_{D-1,\alpha_{K-1}}) \quad (30)$$

$$= \mathbf{V}\mathbf{U}, \quad (31)$$

where \mathbf{U} is an upper triangular matrix obtained from the orthogonalization process. Note that we continue to label the orthonormal vectors using the original indices (j, α_k) .

The top and bottom panels of Fig. 1 respectively show the template basis $v_{j,\alpha_k}^I(t)$ presented in Eqs. (9)–(12) and the orthonormal template basis $\tilde{v}_{j,\alpha_k}^I(t)$ obtained through the orthogonalization procedure described above. Compared to the original basis, the orthonormal basis functions appear more distinct from one another, indicating that they form a more independent set and are thus expected to provide a more efficient representation of ring-down signal. Note that $\tilde{v}_{j,\alpha_k}^I(t)$ scales with the noise level, as it is normalized using the inner product (29) defined by the noise correlation matrix \mathbf{R} .

By construction, the new basis vectors satisfy

$$\tilde{\mathbf{V}}^T \mathbf{R}^{-1} \tilde{\mathbf{V}} = \mathbb{I}. \quad (32)$$

In terms of the orthonormal basis, the likelihood takes the following form,

$$\ln \mathcal{L}(\boldsymbol{\theta}) = \tilde{\mathbf{d}}^T \tilde{\mathbf{c}} - \frac{1}{2} \tilde{\mathbf{c}}^T \tilde{\mathbf{c}} + \text{const.}, \quad (33)$$

where

$$\tilde{\mathbf{d}} = \tilde{\mathbf{V}}^T \mathbf{R}^{-1} \mathbf{d}, \quad \tilde{\mathbf{c}} = \mathbf{U}^{-1} \mathbf{c}. \quad (34)$$

This expression shows that the likelihood function is Gaussian in $\tilde{\mathbf{c}}$ with diagonal covariance. In contrast, Eq. (28) shows that the likelihood is Gaussian in \mathbf{c} with covariance of $(\mathbf{V}^T \mathbf{R}^{-1} \mathbf{V})^{-1}$, which generally contains off-diagonal terms. Thus, the transformation reduces parameter correlations in the posterior. This advantage is further demonstrated through simulation studies presented in later sections.

The orthonormal vectors for α_k with $k > 0$ span the subspace orthogonal to all basis vectors associated with earlier modes $\{\alpha_{k'}\}_{k' < k}$. As a result, they isolate components that cannot be represented by earlier modes but are present in the α_k -modes. As explained in a later section, we use nonzero values of \tilde{c}_{j,α_k} to infer the presence of the α_k -modes in data.

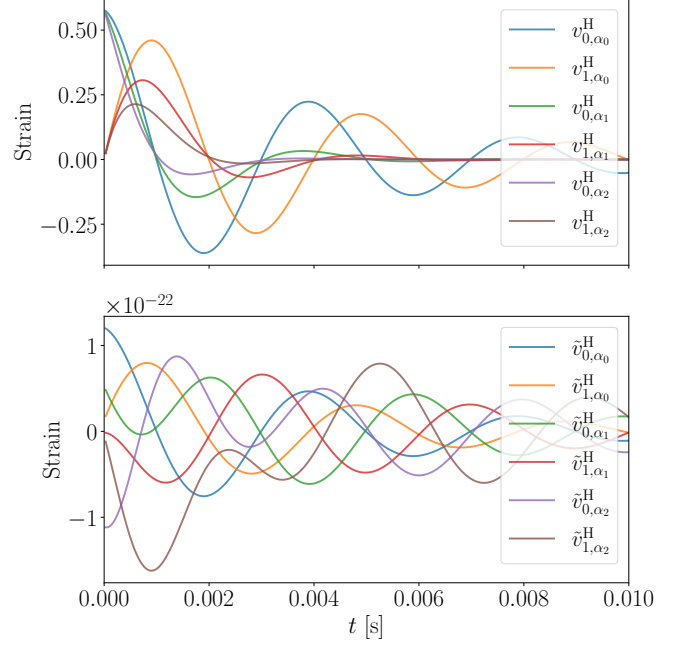


FIG. 1. The top panel shows the template basis composed of the original (non-orthogonal) modes $v_{j,\alpha_k}^I(t)$, as presented in Eqs. (9)–(12). We fix $M_f = 68.2 M_\odot$, $\chi_f = 0.692$, and $t_S^I = 0$. The bottom panel shows the orthonormal template basis $\tilde{v}_{j,\alpha_k}^I(t)$ obtained by orthogonalizing the original basis. Here, we adopt the noise PSD estimated with the data around GW150914, available from Ref. [38]. We focus solely on the $l = m = 2$ modes with $D = 2$ and include up to the second overtone, fixing the detector I to Hanford. The detector beam pattern functions are evaluated with the fixed values: right ascension of 1.95 rad, declination of -1.27 rad, polarization angle of 0.82 rad, and reference GPS time of 1126259462.423 s.

B. Marginalization over mode amplitudes

One of the key advantages of using orthonormal basis vectors is that, under a prior that is uniform in the mode amplitudes, the posterior can be analytically marginalized over the mode coefficients. We define the amplitude of α_k -modes as

$$\tilde{A}_{\alpha_k} \equiv \sqrt{\sum_{j=0}^{D-1} (\tilde{c}_{j,\alpha_k})^2}. \quad (35)$$

With these mode amplitudes, the likelihood function is expressed as

$$\mathcal{L} \propto \prod_k \mathcal{L}_{\alpha_k}, \quad (36)$$

$$\mathcal{L}_{\alpha_k} \equiv \exp \left[-\frac{1}{2} \tilde{A}_{\alpha_k}^2 + \tilde{A}_{\alpha_k} \tilde{d}_{\alpha_k} \cos \beta_{\alpha_k} \right].$$

Here, \tilde{d}_{α_k} and β_{α_k} denote the L^2 norm of $\tilde{\mathbf{d}}_{\alpha_k}$ and the angle between $\tilde{\mathbf{d}}_{\alpha_k}$ and $\tilde{\mathbf{c}}_{\alpha_k}$, respectively, where $\tilde{\mathbf{d}}_{\alpha_k}$ and

$\tilde{\mathbf{c}}_{\alpha_k}$ are the subvectors of $\tilde{\mathbf{d}}$ and $\tilde{\mathbf{c}}$ collecting the components associated with the α_k -modes. The prior uniform in the mode amplitudes is given by

$$\pi(\{c_{j,\alpha_k}\}) \prod_{j,k} dc_{j,\alpha_k} \propto \prod_k \frac{1}{\tilde{A}_{\alpha_k}^{D-1}} \prod_{j,k} d\tilde{c}_{j,\alpha_k}. \quad (37)$$

With this prior, the likelihood for a single mode, \mathcal{L}_{α} , can be analytically marginalized over the mode coefficients. The likelihood marginalized over the coefficients with the mode amplitude fixed is proportional to

$$\begin{aligned} \mathcal{L}_{\alpha}^{\beta} &\equiv \int_0^{\pi} \sin^{D-2} \beta_{\alpha} d\beta_{\alpha} \mathcal{L}_{\alpha} \\ &= 2^{\frac{D}{2}-1} \sqrt{\pi} \Gamma\left(\frac{D-1}{2}\right) \times \\ &\quad (\tilde{A}_{\alpha} \tilde{d}_{\alpha})^{-\frac{D}{2}} e^{-\frac{\tilde{A}_{\alpha}^2}{2}} \left(D I_{\frac{D}{2}}(\tilde{A}_{\alpha} \tilde{d}_{\alpha}) + \tilde{A}_{\alpha} \tilde{d}_{\alpha} I_{\frac{D+2}{2}}(\tilde{A}_{\alpha} \tilde{d}_{\alpha}) \right). \\ &= \begin{cases} \pi e^{-\frac{\tilde{A}_{\alpha}^2}{2}} I_0(\tilde{A}_{\alpha} \tilde{d}_{\alpha}) & (D=2), \\ \pi e^{-\frac{\tilde{A}_{\alpha}^2}{2}} (\tilde{A}_{\alpha} \tilde{d}_{\alpha})^{-1} I_1(\tilde{A}_{\alpha} \tilde{d}_{\alpha}) & (D=4), \end{cases} \end{aligned} \quad (38)$$

where $I_n(z)$ is the modified Bessel function of the first kind. Finally, marginalizing over the mode amplitude yields

$$\begin{aligned} \mathcal{L}_{\alpha}^{A,\beta} &\equiv \int_0^{\infty} d\tilde{A}_{\alpha} \mathcal{L}_{\alpha}^{\beta} \\ &= \frac{\pi}{4\sqrt{2}} \Gamma\left(\frac{D-1}{2}\right) \left[2D_1 F_1^R\left(\frac{1}{2}, \frac{D}{2} + 1, \frac{\tilde{d}_{\alpha}^2}{2}\right) + \right. \\ &\quad \left. \tilde{d}_{\alpha}^2 F_1^R\left(\frac{3}{2}, \frac{D}{2} + 2, \frac{\tilde{d}_{\alpha}^2}{2}\right) \right] \\ &= \begin{cases} \frac{\pi^{\frac{3}{2}}}{\sqrt{2}} e^{\frac{\tilde{d}_{\alpha}^2}{4}} I_0\left(\frac{\tilde{d}_{\alpha}^2}{4}\right) & (D=2), \\ \frac{\pi^{\frac{3}{2}}}{2\sqrt{2}} e^{\frac{\tilde{d}_{\alpha}^2}{4}} \left[I_0\left(\frac{\tilde{d}_{\alpha}^2}{4}\right) - I_1\left(\frac{\tilde{d}_{\alpha}^2}{4}\right) \right] & (D=4), \end{cases} \end{aligned} \quad (40)$$

where ${}_pF_q^R(z)$ is the regularized confluent hypergeometric function.

By performing analytic marginalization, we avoid the need to explore the KD -dimensional coefficient space with a numerical method such as Markov chain Monte Carlo (MCMC) methods. This approach significantly reduces the computational cost of the analysis, especially when a large number of QNMs are considered. Moreover, it naturally accounts for the entire range of coefficient values from $-\infty$ to ∞ , which is not easily achieved with standard numerical techniques.

C. Sampling procedure

The sampling procedure of our semi-analytic method proceeds as follows. With the analytic marginalization

described above, the marginal posterior for the remnant BH's mass and spin can be computed as

$$p(M_f, \chi_f) \propto \pi(M_f, \chi_f) \prod_{\alpha} \mathcal{L}_{\alpha}^{A,\beta}. \quad (41)$$

Samples of (M_f, χ_f) can then be generated numerically from this posterior distribution.

For each sampled pair (M_f, χ_f) , the mode amplitude \tilde{A}_{α_k} is drawn from the conditional distribution,

$$p(\tilde{A}_{\alpha_k} | M_f, \chi_f) = \frac{p(M_f, \chi_f, \tilde{A}_{\alpha_k})}{p(M_f, \chi_f)} \propto \mathcal{L}_{\alpha_k}^{\beta}. \quad (42)$$

Finally, for each sampled pair $(M_f, \chi_f, \tilde{A}_{\alpha_k})$, the angular parameters of the $(D-1)$ -dimensional unit sphere are sampled from the likelihood \mathcal{L}_{α_k} , and the mode coefficients $\{c_{j,\alpha_k}\}$ are reconstructed accordingly.

D. Mode identification

One of the goals of our semi-analytic method is to efficiently identify subdominant QNMs associated with α_k for $k > 0$. As described in Sec. III A, the orthonormal vectors corresponding to α_k isolate distinct signal features introduced by the α_k -modes. We infer the presence of these modes in the data through their non-zero projection coefficients. More formally, we consider a mode detected when the marginal posterior $p(\tilde{A}_{\alpha_k})$ excludes $\tilde{A}_{\alpha_k} = 0$ with a specified credibility level (e.g. 90%). While credible intervals can be constructed in various ways, we adopt the highest posterior density (HPD) interval, defined as the smallest continuous interval containing the desired posterior mass.

A similar approach to identify subdominant modes was proposed in [36]. Their method involves performing multiple analyses, incrementally adding new modes, and stopping once the added modes are not identified with a specified credibility level. In contrast, since our method reduces correlations between modes, we infer the presence of the modes with a single analysis including all the modes we are interested in, or at least with fewer analyses.

Another common strategy is to use the Bayes factor to compare models with different numbers of modes. As noted by Isi et al., this approach is meaningful only when the prior accurately reflects our beliefs about the parameters. However, because we lack strong prior knowledge about the mode coefficients and allow them to take arbitrary real values, we choose not to use this method.

IV. APPLICATION TO DAMPED SINUSOIDS

To evaluate the performance of the analysis using orthonormal modes, we apply it to mock data generated by summing damped sinusoids, as described by Eq. (13).

The frequencies and decay times of the damped sinusoids are set to those of Kerr QNMs with the BH parameters of $M_f = 68.2 M_\odot$ and $\chi_f = 0.692$, consistent with those inferred from GW150914. Precise calculations of complex QNM frequencies at discrete spin values are provided in [39, 40]. We interpolate their results to compute QNM frequencies and decay times for both signal injection and parameter inference.

We simulate damped-sinusoidal signals observed by the two LIGO detectors at Hanford and Livingston. The simulations are performed under the “zero-noise” assumption, where the simulated signals are assumed to be observed in the absence of random detector noise. The sampling rate of data is 2048 Hz, and the duration of analyzed data is $300M$, where $M = 68.2 M_\odot$. The covariance matrix is constructed using the noise PSD estimated with the data around GW150914, available from Ref. [38]. The right ascension, declination, and polarization angle are set to values consistent with those of GW150914: $\alpha = 1.95$ rad, $\delta = -1.27$ rad, and $\psi = 0.82$ rad. The start time of the damped sinusoids measured at the Earth’s center, which we refer to as the peak time t_{peak} , is also chosen to match GW150914: $t_{\text{peak}} = 1126259462.423$ s, expressed in GPS time.

The simulated signals include only $l = m = 2$ modes. We consider two types of signals: one including four modes up to $n = 3$, and another including eight modes up to $n = 7$. These are referred to as the 4-mode and 8-mode signals, respectively. The mode coefficients assumed in these simulations are listed in Tabs. I and II. For the 4-mode signal, the coefficients are chosen to mimic the post-merger phase of SXS:BBH:0305. For the 8-mode signal, the coefficients are computed based on the results presented in Table I of [29], which were obtained by fitting QNMs to a numerical waveform from the SXS catalog. Those coefficients are normalized to achieve a network signal-to-noise ratio (SNR) of 30. Each simulated signal is analyzed assuming the same set of QNMs that is used to construct the corresponding simulated signal. Unless otherwise specified, the analysis assumes $D = 4$ damped sinusoids per QNM. All analyses are performed starting from the peak time of the signal. The true values of right ascension and declination are used to compute the peak time at each detector and the detector beam patterns.

TABLE I. Injected values of the mode coefficients c_{j,α_k} for the 4-mode signal. The listed values are scaled by 10^{-20} . The coefficients are chosen to mimic the post-merger phase of SXS:BBH:0305 and to achieve a network SNR of 30.

k	c_{0,α_k}	c_{1,α_k}	c_{2,α_k}	c_{3,α_k}
0	-0.4768	0.8502	-0.3376	-0.3609
1	2.0116	-0.7439	-0.2217	0.7646
2	-0.4013	-0.0456	0.2399	-0.0094
3	-0.7062	-0.1697	0.1110	-0.0951

For comparison, we also perform an analysis with flat priors on the amplitude of the original (non-orthogonal)

TABLE II. Injected values of the coefficients $c_{j,\alpha}$ for the 8-mode signal. The Listed values are scaled by 10^{-20} . The coefficients are chosen to mimic the post-merger phase of SXS:BBH:0305 and to achieve a network SNR of 30. Note that there exist relations among the coefficients, such as $c_{0,\alpha_k} = -c_{3,\alpha_k}$ and $c_{1,\alpha_k} = c_{2,\alpha_k}$, which correspond to the case of circular polarization.

k	c_{0,α_k}	c_{1,α_k}	c_{2,α_k}	c_{3,α_k}
0	0.1155	-1.2096	-1.2096	-0.1155
1	4.1100	3.2590	3.2590	-4.1100
2	-13.5496	-3.7801	-3.7801	13.5496
3	27.3075	7.6071	7.6071	-27.3075
4	-35.6762	-19.3948	-19.3948	35.6762
5	25.5084	25.8310	25.8310	-25.5084
6	-8.4943	-15.5784	-15.5784	8.4943
7	1.1162	3.4913	3.4913	-1.1162

modes:

$$A_{\alpha_k} \equiv \sqrt{\sum_{j=0}^{D-1} (c_{j,\alpha_k})^2}. \quad (43)$$

In this analysis, the amplitude prior is taken to be uniform over a finite range, $(0, 2.5 \times 10^{-19})$, and we use the Metropolis–Hastings sampler as implemented in the Python package PyMC [41] to draw samples from the posterior distribution. In both analyses, we adopt uniform priors for mass and spin as $M_f/M_\odot \sim \mathcal{U}(40, 100)$ and $\chi_f \sim \mathcal{U}(0, 0.99)$, respectively.

A. Results

Figure 2 shows the posterior distributions of the remnant BH’s mass, spin, and mode amplitudes obtained by analyzing the 4-mode signal. The left panel presents the results from our semi-analytic method, while the right panel shows the reference MCMC analysis. As seen in the right panel, A_{221} and A_{222} are anti-correlated, and the probability of both vanishing simultaneously is small. More quantitatively, the hypothesis $A_{221} = A_{222} = 0$ is excluded at the 99% credible level. However, the fact that one of them is likely not zero is not apparent in either of their one-dimensional distributions, as neither excludes $A_{221} = 0$ nor $A_{222} = 0$. On the other hand, in the posterior distributions obtained from our semi-analytic method, the one-dimensional posterior distribution of \tilde{A}_{221} excludes $\tilde{A}_{221} = 0$ from the 97.6% HPD credible region, indicating that the $(2, 2, 1)$ mode can be extracted from the data based solely on the one-dimensional marginal distribution.

Figure 3 shows the result of analyzing the 4-mode signal assuming $D = 2$ damped sinusoids per QNM. The posterior distributions obtained assuming $D = 2$ qualitatively resemble those obtained assuming $D = 4$. Because the two LIGO detectors are nearly co-aligned, as discussed in Sec. II, the signal model with $D = 2$ can

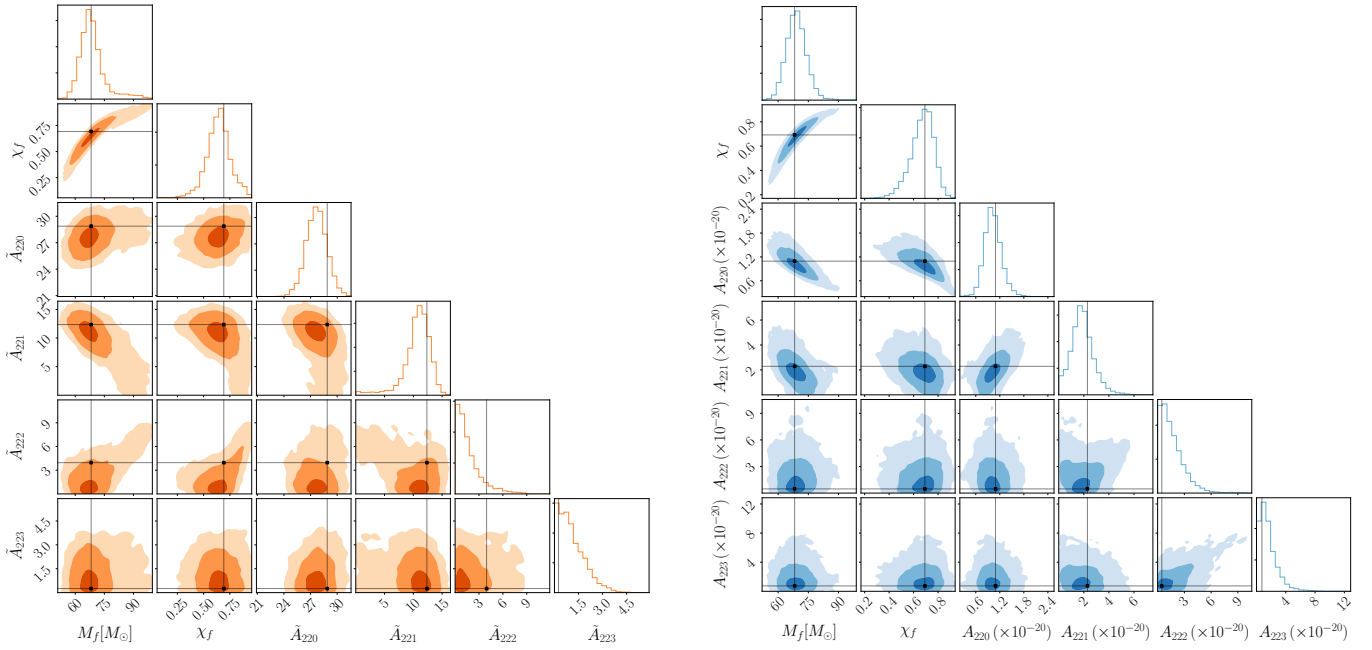


FIG. 2. Posterior distributions for the remnant BH's mass, spin, and mode amplitudes obtained by analyzing the 4-mode signal. The left (right) panel shows the results from the semi-analytic (MCMC) method. The contours are color-coded to represent the 1- σ (39.3%), 2- σ (86.5%), and 3- σ (98.9%) credible regions. The black lines represent the injected values.

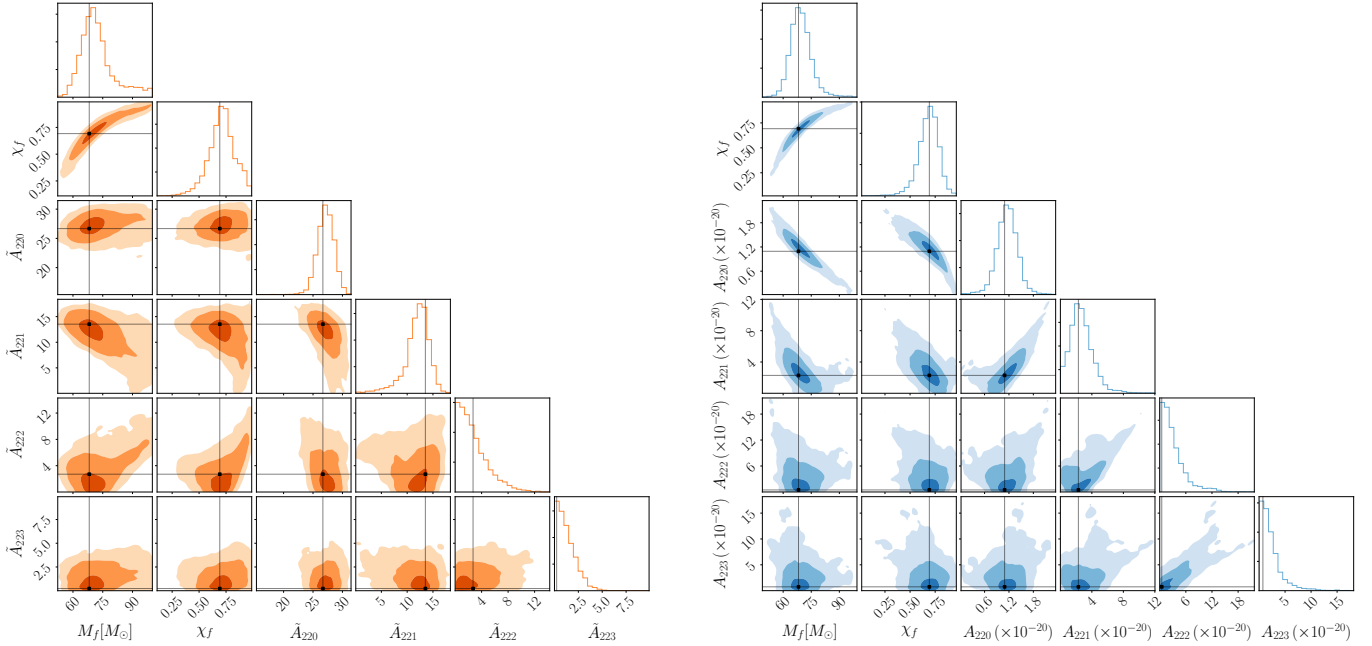


FIG. 3. Posterior distributions for mass, spin, and mode amplitudes obtained by analyzing the 4-mode signal under the assumption of $D = 2$ damped sinusoids per QNM. The left (right) panel shows the results from the semi-analytic (MCMC) method.

describe the observed signal with sufficient accuracy. In the $D = 2$ MCMC analysis, we observe strong positive correlations between amplitude parameters, such as between A_{222} and A_{223} . These modes tend to be out of phase so that they cancel each other out in the resulting waveform. As seen in the results for $D = 4$, the corre-

lations between the amplitude parameters are mitigated with our semi-analytic method, and the one-dimensional posterior distribution of \tilde{A}_{221} excludes $\tilde{A}_{221} = 0$ at the 99.7% credibility.

As the number of modes in the template increases, correlations between mode amplitudes become more severe.

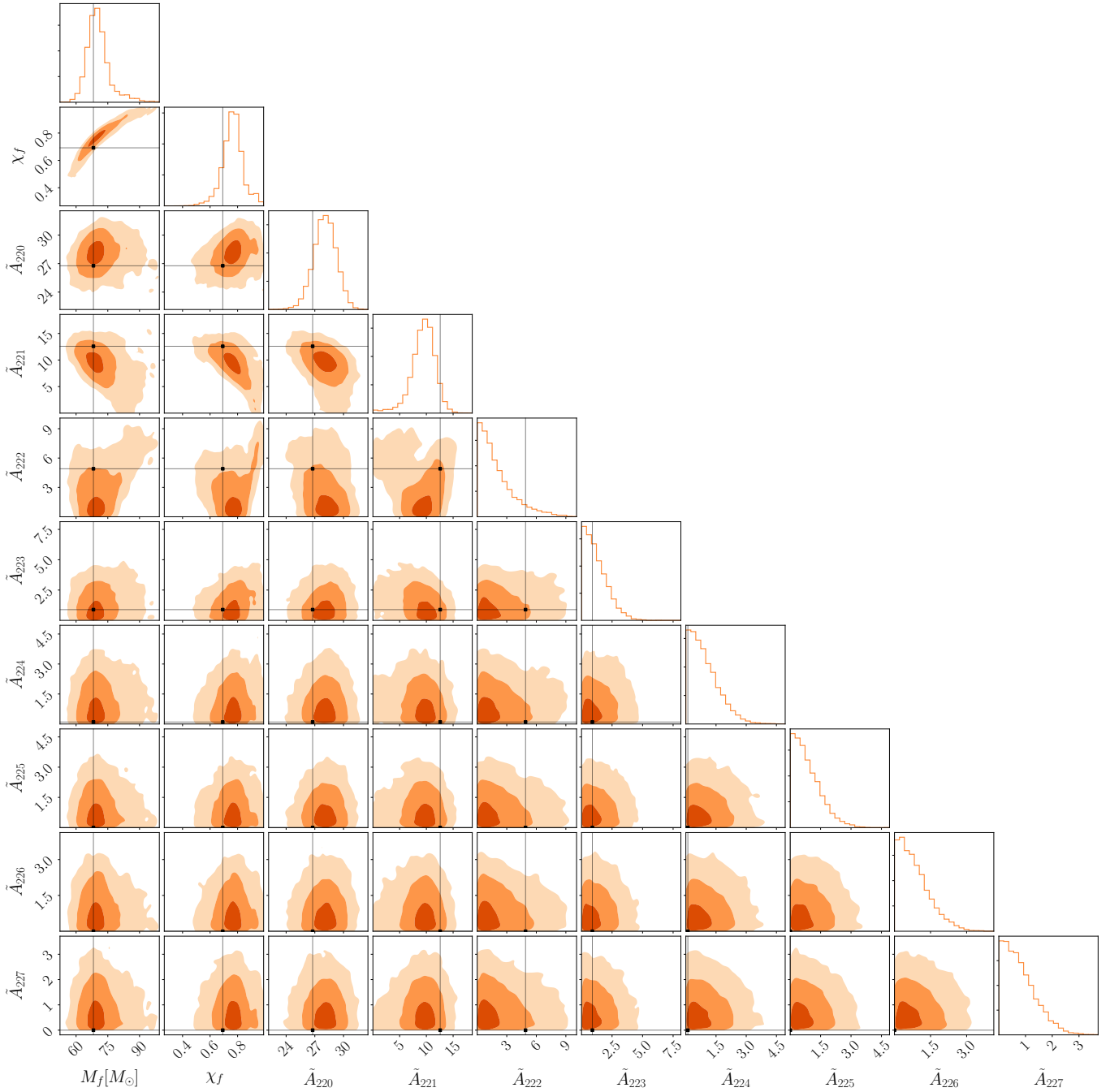


FIG. 4. Posterior distributions for mass, spin, and mode amplitudes obtained from the semi-analytic method by analyzing the 8-mode signal. The analysis starts from the peak time.

This tends to lead to strong degeneracies between the different mode amplitudes, making it difficult to extract individual mode amplitudes in a robust way [42]. Figure 4 shows the results obtained by applying our semi-analytic method to the 8-mode signal. Even with a large number of modes, the amplitude parameters of the orthogonal modes remain only weakly correlated. The one-dimensional posterior distribution of \tilde{A}_{221} excludes $\tilde{A}_{221} = 0$ at the 99.5% credibility.

We also observe that the peak of the marginal posterior distribution for M_f and χ_f is off from their true values. Although the likelihood function is maximized at the true parameter values in the zero-noise simulation, the marginal posterior does not necessarily peak at those values. In our case, the product of the terms involving the Bessel functions in Eq. (40) taken over different α_k does not necessarily get maximized at the true values of M_f and χ_f . This accounts for the observed shift in the

marginal posterior.

B. Reweighting for different prior choices

In principle, we can obtain the samples under a flat prior on $\{A_{\alpha_k}\}$ by reweighting samples generated under a flat prior on $\{\tilde{A}_{\alpha_k}\}$ employing the rejection sampling or importance sampling techniques. The sampling procedure proceeds as follows: First, generate a sample set $\{M_f, \chi_f, \{\tilde{c}_{i,\alpha_k}\}\}$ using our semi-analytic method. Then, convert $\{\tilde{c}_{j,\alpha_k}\}$ into $\{c_{j,\alpha_k}\}$ using the inverse of Eq. (34), evaluated at the corresponding $\{M_f, \chi_f\}$. Finally, perform rejection or importance sampling by assigning the following weight to each sample:

$$w = |\det U| \prod_{0 \leq k \leq K-1} \left(\frac{A_{\alpha_k}}{\tilde{A}_{\alpha_k}} \right)^{D-1}. \quad (44)$$

However, this reweighting becomes increasingly inefficient as the number of QNMs grows. More critically, the weight w generally diverges if $\tilde{A}_{\alpha_k} = 0$ for any k . Figure 5 shows the results of applying importance sampling to the 4-mode signal assuming $D = 2$, in comparison with the results from the reference MCMC analysis. The importance sampling is performed using 10^5 samples. While the resultant posterior qualitatively agrees with that of the reference MCMC, the two differ by more than what can be explained by statistical errors. Nevertheless, due to its speed and ease of parallelization, the semi-analytic method combined with rejection or importance sampling can be a useful approach, particularly when the number of QNMs considered is small.

V. APPLICATION TO BINARY BLACK HOLE WAVEFORMS

Next, we apply our semi-analytic method to the numerical-relativity waveform provided in the latest SXS catalog (v3.0.0) [43]. Specifically, we employ the waveform from the SXS:BBH:0305 simulation, which models a non-precessing BBH merger with a mass ratio of 1.22 and a dimensionless spin magnitude of 0.692, parameter values consistent with those inferred from GW150914. We set the other parameters such as detector-frame final mass M_f , peak time measured at the Earth's center t_{peak} , luminosity distance d_L , right ascension α , declination δ , polarization angle ψ , inclination angle ι , and constant phase ϕ to the values consistent with those inferred from GW150914:

$$\begin{aligned} M_f &= 68.2 M_\odot, & d_L &= 390 \text{ Mpc}, \\ \alpha &= 1.95 \text{ rad}, & \delta &= -1.27 \text{ rad}, & \psi &= 0.82 \text{ rad}, \\ \iota &= 0, & \phi &= 0, & t_{\text{peak}} &= 1126259462.423 \text{ s}. \end{aligned}$$

The peak time is defined as the time at which $|h_+(t)|^2 + |h_\times(t)|^2$ gets maximized. The simulated signal only con-

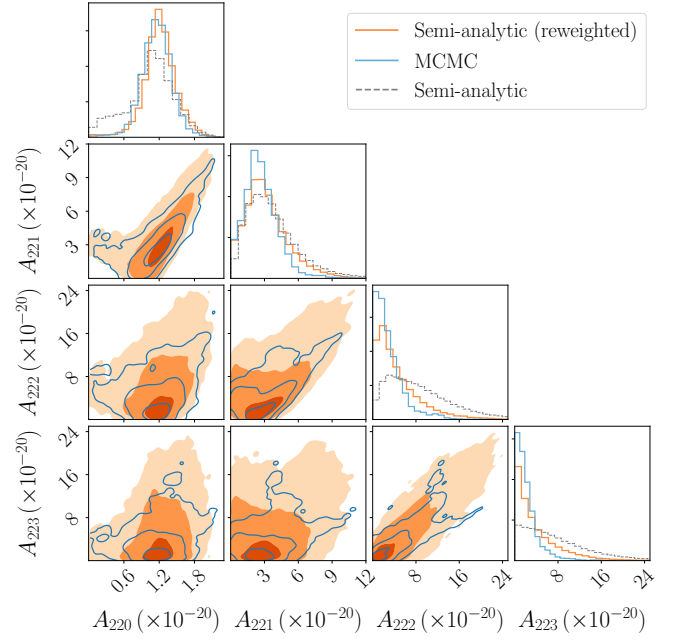


FIG. 5. Comparison of posterior distributions obtained by reweighting samples from our semi-analytic method (orange filled contours) and those from the reference MCMC method (blue lines). The gray dashed lines represent one-dimensional posteriors of the original samples from our semi-analytic method. The results are obtained from the analysis of the 4-mode signal assuming $D = 2$ damped sinusoids per QNM. The contours represent the 1- σ (39.3%), 2- σ (86.5%), and 3- σ (98.9%) credible regions.

tains the $l = |m| = 2$ spherical harmonic modes from the SXS:BBH:0305 dataset.

As in the previous section, we perform zero-noise simulations. We assume a two-detector network consisting of the LIGO Hanford and Livingston. We consider four representative sensitivity curves: the noise PSD estimated with the data around GW150914 [38], the design sensitivity for the O4 [44], the anticipated design sensitivity for the fifth observing run (O5) (A_+ sensitivity) [45], and the proposed $A_\#$ sensitivity for future upgrades [46]. The sampling rate of the data is 2048 Hz, and the duration of the analyzed data is $300M$, where $M = 68.2 M_\odot$.

We adopt uniform priors for mass and spin as $M_f/M_\odot \sim \mathcal{U}(40, 100)$ and $\chi_f \sim \mathcal{U}(0, 0.9)$, respectively. The analysis start time at each detector is set to $5M$ after the peak time, where $M = 68.2 M_\odot$. As in the previous section, we use the complex QNM frequencies provided in [39, 40] to compute QNM frequencies and decay times. The analysis takes into account QNMs with $(l, m, n) = (2, 2, 0), (2, 2, 1), (2, 2, 2)$ and $D = 2$ damped sinusoids per QNM. As we do in the previous section, we perform an MCMC analysis using flat priors on the original mode amplitudes for comparison. The amplitude prior is assumed to be uniform over $(0, 2.5 \times 10^{-19})$, and we use the same sampler as in the previous section to draw samples.

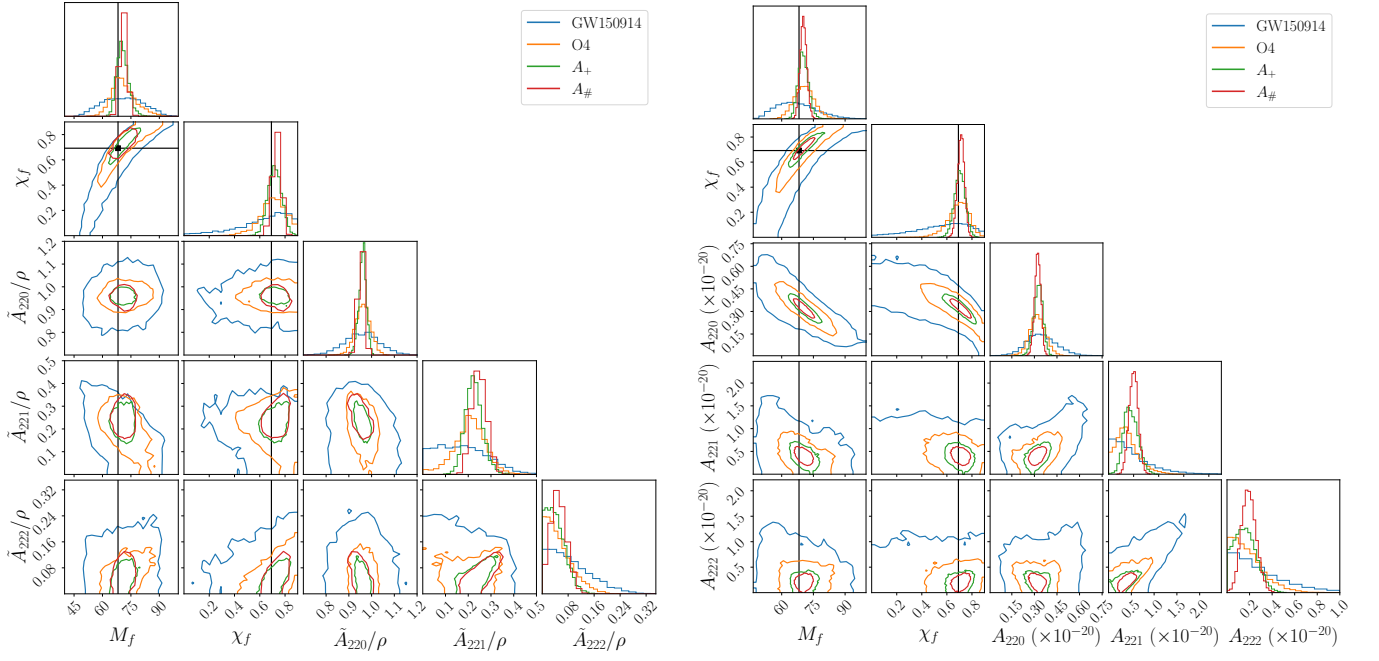


FIG. 6. Posterior distributions for mass, spin, and mode amplitudes, evaluated using the $l = |m| = 2$ spherical harmonic modes from SXS:BBH:0305. The analysis start time at each detector is set to $5M$ after the peak time, where $M = 68.2 M_\odot$. The left panel shows the results obtained from our semi-analytic method. By definition, the quantity \tilde{A}_{α_k} is normalized by the detector noise. Therefore, the values of the mode amplitude are scaled by dividing by the post-peak SNR ρ corresponding to each detector sensitivity. The right panel shows the results obtained from the reference MCMC method. The blue, orange, green, and red lines present the results assuming the noise PSD estimated using the data around GW150914, the design sensitivity for the O4, the A_+ sensitivity, and the $A_\#$ sensitivity, respectively. The contours represent 90% credible regions.

Figure 6 shows the posterior distributions for each detector sensitivity, where the left and right panels show the results from our semi-analytic method and the reference MCMC method, respectively. By construction, \tilde{A}_α represents the amplitude of the template normalized by the detector noise. Taking this effect into account, we present the mode amplitudes normalized by the SNR ρ for each detector sensitivity.

Comparing the left and right panels of Fig. 6, we observe that, as confirmed by the analyses of damped sinusoids, the use of orthonormal modes reduces correlations between modes—for example, between $(2, 2, 0)$ and $(2, 2, 1)$. This allows us to identify subdominant modes from their one-dimensional distributions with high credibility. For example, the one-dimensional posterior distribution of A_{221} assuming the O4 sensitivity shows that the hypothesis $A_{221} = 0$ is disfavored at the 80% credible level. On the other hand, when the semi-analytic method is used, the reduced correlation leads to the hypothesis $\tilde{A}_{221} = 0$ being rejected at the 98% credible level. These results demonstrate that our semi-analytic method is effective for identifying subdominant QNMs from BBH signals.

VI. CONCLUSION

In this paper, we propose an efficient Bayesian method for identifying multiple QNMs in GWs from BBH mergers. Our approach applies the Gram-Schmidt algorithm to the QNM basis to construct orthonormal modes, thereby reducing correlations among them. This reduction in correlation is demonstrated through numerical experiments presented in Sections IV and V. By adopting a prior that is uniform over the amplitudes of the orthonormal modes, we enable analytical marginalization over the amplitudes, which significantly reduces the computational cost. Our method is particularly well suited for analyzing future BBH events with high SNRs, where the detection of multiple QNMs is more likely.

The identification of overtones with less correlation would be especially valuable for high-spin Kerr ringdowns, where the QNM frequencies of the overtones get close. It would be interesting to apply our method to this regime and investigate extraction of resonant excitations near exceptional points [39].

While this work focuses on mode identification, once multiple QNMs are observed, the next step is to test GR by checking the consistency of their frequencies and damping times. Previous studies have addressed this by introducing additional parameters to allow the frequencies and damping times of subdominant modes to deviate

from their GR-predicted values [16, 47, 48]. The extension of our method to accommodate such analyses is a future work.

Another promising direction is the application of our method to real data. It would be interesting to revisit existing events, such as GW150914, to investigate the significance of subdominant modes with our method. With future improvements in detector sensitivity, BBH events with higher SNRs will become more common, making our method increasingly valuable for such analyses.

ACKNOWLEDGMENTS

We thank Hiroyuki Nakano for careful reading of the manuscript and helpful comments. This work was supported by Japan Society for the Promotion of Science (JSPS) Grants-in-Aid for Transformative Research Areas (A) No. 23H04891 and No. 23H04893 (SM), JSPS Grant-in-Aid for Scientific Research (KAKENHI) Grant No. JP22K03639 (HM), and JSPS KAKENHI grant No. 23KJ06945 (DW).

-
- [1] B. P. Abbott et al. (LIGO Scientific, Virgo), *Phys. Rev. X* **9**, 031040 (2019), [arXiv:1811.12907 \[astro-ph.HE\]](#).
 - [2] R. Abbott et al. (LIGO Scientific, Virgo), *Phys. Rev. X* **11**, 021053 (2021), [arXiv:2010.14527 \[gr-qc\]](#).
 - [3] R. Abbott et al. (LIGO Scientific, VIRGO), *Phys. Rev. D* **109**, 022001 (2024), [arXiv:2108.01045 \[gr-qc\]](#).
 - [4] R. Abbott et al. (KAGRA, VIRGO, LIGO Scientific), *Phys. Rev. X* **13**, 041039 (2023), [arXiv:2111.03606 \[gr-qc\]](#).
 - [5] B. P. Abbott et al. (LIGO Scientific, Virgo), *Phys. Rev. Lett.* **116**, 221101 (2016), [Erratum: *Phys.Rev.Lett.* 121, 129902 (2018)], [arXiv:1602.03841 \[gr-qc\]](#).
 - [6] B. P. Abbott et al. (LIGO Scientific, Virgo), *Phys. Rev. Lett.* **123**, 011102 (2019), [arXiv:1811.00364 \[gr-qc\]](#).
 - [7] B. P. Abbott et al. (LIGO Scientific, Virgo), *Phys. Rev. D* **100**, 104036 (2019), [arXiv:1903.04467 \[gr-qc\]](#).
 - [8] F. Echeverria, *Phys. Rev. D* **40**, 3194 (1989).
 - [9] S. A. Hughes and K. Menou, *Astrophys. J.* **623**, 689 (2005), [arXiv:astro-ph/0410148](#).
 - [10] A. Ghosh et al., *Phys. Rev. D* **94**, 021101 (2016), [arXiv:1602.02453 \[gr-qc\]](#).
 - [11] A. Ghosh, N. K. Johnson-Mcdaniel, A. Ghosh, C. K. Mishra, P. Ajith, W. Del Pozzo, C. P. L. Berry, A. B. Nielsen, and L. London, *Class. Quant. Grav.* **35**, 014002 (2018), [arXiv:1704.06784 \[gr-qc\]](#).
 - [12] O. Dreyer, B. J. Kelly, B. Krishnan, L. S. Finn, D. Garrison, and R. Lopez-Aleman, *Class. Quant. Grav.* **21**, 787 (2004), [arXiv:gr-qc/0309007](#).
 - [13] E. Berti, V. Cardoso, and C. M. Will, *Phys. Rev. D* **73**, 064030 (2006), [arXiv:gr-qc/0512160](#).
 - [14] E. Berti, J. Cardoso, V. Cardoso, and M. Cavaglia, *Phys. Rev. D* **76**, 104044 (2007), [arXiv:0707.1202 \[gr-qc\]](#).
 - [15] E. Berti et al., (2025), [arXiv:2505.23895 \[gr-qc\]](#).
 - [16] M. Isi, M. Giesler, W. M. Farr, M. A. Scheel, and S. A. Teukolsky, *Phys. Rev. Lett.* **123**, 111102 (2019), [arXiv:1905.00869 \[gr-qc\]](#).
 - [17] C. D. Capano, M. Cabero, J. Westerweck, J. Abedi, S. Kasta, A. H. Nitz, Y.-F. Wang, A. B. Nielsen, and B. Krishnan, *Phys. Rev. Lett.* **131**, 221402 (2023), [arXiv:2105.05238 \[gr-qc\]](#).
 - [18] H. Siegel, M. Isi, and W. M. Farr, *Phys. Rev. D* **108**, 064008 (2023), [arXiv:2307.11975 \[gr-qc\]](#).
 - [19] B. P. Abbott et al. (LIGO Scientific, Virgo), *Phys. Rev. Lett.* **116**, 061102 (2016), [arXiv:1602.03837 \[gr-qc\]](#).
 - [20] K. Wang, *Eur. Phys. J. C* **82**, 125 (2022), [arXiv:2111.00953 \[gr-qc\]](#).
 - [21] R. Cotesta, G. Carullo, E. Berti, and V. Cardoso, *Phys. Rev. Lett.* **129**, 111102 (2022), [arXiv:2201.00822 \[gr-qc\]](#).
 - [22] E. Finch and C. J. Moore, *Phys. Rev. D* **106**, 043005 (2022), [arXiv:2205.07809 \[gr-qc\]](#).
 - [23] S. Ma, L. Sun, and Y. Chen, *Phys. Rev. Lett.* **130**, 141401 (2023), [arXiv:2301.06705 \[gr-qc\]](#).
 - [24] A. Correia, Y.-F. Wang, J. Westerweck, and C. D. Capano, *Phys. Rev. D* **110**, L041501 (2024), [arXiv:2312.14118 \[gr-qc\]](#).
 - [25] H.-T. Wang, Z. Wang, Y. Dong, G. Yim, and L. Shao, *Phys. Rev. D* **111**, 064037 (2025), [arXiv:2411.13333 \[gr-qc\]](#).
 - [26] V. Baibhav, M. H.-Y. Cheung, E. Berti, V. Cardoso, G. Carullo, R. Cotesta, W. Del Pozzo, and F. Duque, *Phys. Rev. D* **108**, 104020 (2023), [arXiv:2302.03050 \[gr-qc\]](#).
 - [27] P. J. Nee, S. H. Völkel, and H. P. Pfeiffer, *Phys. Rev. D* **108**, 044032 (2023), [arXiv:2302.06634 \[gr-qc\]](#).
 - [28] M. H.-Y. Cheung, E. Berti, V. Baibhav, and R. Cotesta, *Phys. Rev. D* **109**, 044069 (2024), [Erratum: *Phys.Rev.D* 110, 049902 (2024)], [arXiv:2310.04489 \[gr-qc\]](#).
 - [29] K. Takahashi and H. Motohashi, *Class. Quant. Grav.* **41**, 195023 (2024), [arXiv:2311.12762 \[gr-qc\]](#).
 - [30] T. A. Clarke et al., *Phys. Rev. D* **109**, 124030 (2024), [arXiv:2402.02819 \[gr-qc\]](#).
 - [31] M. Giesler et al., *Phys. Rev. D* **111**, 084041 (2025), [arXiv:2411.11269 \[gr-qc\]](#).
 - [32] L. Gao et al., (2025), [arXiv:2502.15921 \[gr-qc\]](#).
 - [33] K. Mitman et al., (2025), [arXiv:2503.09678 \[gr-qc\]](#).
 - [34] Y. Dong, Z. Wang, H.-T. Wang, J. Zhao, and L. Shao, (2025), [arXiv:2502.01093 \[gr-qc\]](#).
 - [35] N. Sago, S. Isoyama, and H. Nakano, *Universe* **7**, 357 (2021), [arXiv:2108.13017 \[gr-qc\]](#).
 - [36] M. Isi and W. M. Farr, (2021), [arXiv:2107.05609 \[gr-qc\]](#).
 - [37] M. Isi, *Class. Quant. Grav.* **40**, 203001 (2023), [arXiv:2208.03372 \[gr-qc\]](#).
 - [38] L. S. Collaboration, “Power Spectral Densities (PSD) release for GWTC-1,” (2019), LIGO-P1900011-v1.
 - [39] H. Motohashi, *Phys. Rev. Lett.* **134**, 141401 (2025), [arXiv:2407.15191 \[gr-qc\]](#).
 - [40] H. Motohashi, “Kerr quasinormal mode frequencies and excitation factors,” (2024), zenodo. Data set.
 - [41] O. Abril-Pla, V. Andreani, C. Carroll, L. Dong, C. Fonesbeck, M. Kochurov, R. Kumar, J. Lao, C. Luhmann, O. Martin, M. Osthege, R. Vieira, T. Wiecki, and R. Zinkov, *PeerJ Computer Science* **9** (2023), 10.7717/peerj-cs.1516.
 - [42] T. A. Clarke, M. Isi, P. D. Lasky, E. Thrane, M. Boyle, N. Deppe, L. E. Kidder, K. Mitman, J. Moxon, K. C. Nelli, W. Throwe, and N. L. Vu, *Physical Review D* **109**

- (2024), [10.1103/physrevd.109.124030](#).
- [43] M. A. Scheel et al., “The *sxs* collaboration’s third catalog of binary black hole simulations,” (2025), [arXiv:2505.13378 \[gr-qc\]](#).
 - [44] L. S. Collaboration, “Updated Advanced LIGO sensitivity design curve,” (2018), [LIGO-T1800044-v5](#).
 - [45] L. S. Collaboration, “Unofficial sensitivity curves (ASD) for aLIGO, Kagra, Virgo, Voyager, Cosmic Explorer, and Einstein Telescope,” (2020), [LIGO-T1500293-v13](#).
 - [46] L. S. Collaboration, “*A# Strain Sensitivity*,” (2023), [LIGO-T2300041-v1](#).
 - [47] R. Abbott et al. (LIGO Scientific, Virgo), [Phys. Rev. D **103**, 122002 \(2021\)](#), [arXiv:2010.14529 \[gr-qc\]](#).
 - [48] R. Abbott et al. (LIGO Scientific, VIRGO, KAGRA), (2021), [arXiv:2112.06861 \[gr-qc\]](#).